Science AAAS

www.sciencemag.org/content/358/6369/1411/suppl/DC1

Supplementary Materials for

Disorder-induced optical transition from spin Hall to random Rashba effect

Elhanan Maguid, Michael Yannai, Arkady Faerman, Igor Yulevich, Vladimir Kleiner, Erez Hasman*

*Corresponding author. Email: mehasman@technion.ac.il

Published 15 December 2017, *Science* **358**, 1411 (2017)
DOI: 10.1126/science.aap8640

This PDF file includes:

Supplementary Text
Figs. S1 to S19
References

1. Disordered geometric phase metasurface: design and fabrication

Figure S1 shows a SEM image of a disordered geometric phase metasurface (DGPM) composed of Si-based building blocks. Each building block is 600x600nm^2 and composed of three nanorods which are designed to operate as a wave-plate, oriented at an angle $\theta_\varepsilon(x,y)$. The Si nanorods are 70nm wide, 300nm high and the distance between adjacent nanorods is 200nm. The diameter of the geometric phase metasurface (GPM) is 200μm. All the metasurfaces were fabricated with these parameters.

<u>DGPM fabrication</u>

The poly-Si thin film with a thickness of 300nm was grown at a temperature of 590°C on a SiO_2 (fused silica) substrate. The photoresist CSAR 6200.09 (Allresist GmbH) with a thickness of 190nm was deposited on the poly-Si film and baked at 150°C for 1 minute. To transfer the pattern onto the poly-Si film, a photoresist mask was made using a Raith EBPG E-beam lithography system, then baked at 130°C for 1 minute and etched using deep reactive-ion etching by F-ICP Plasma Therm system for 30 seconds.

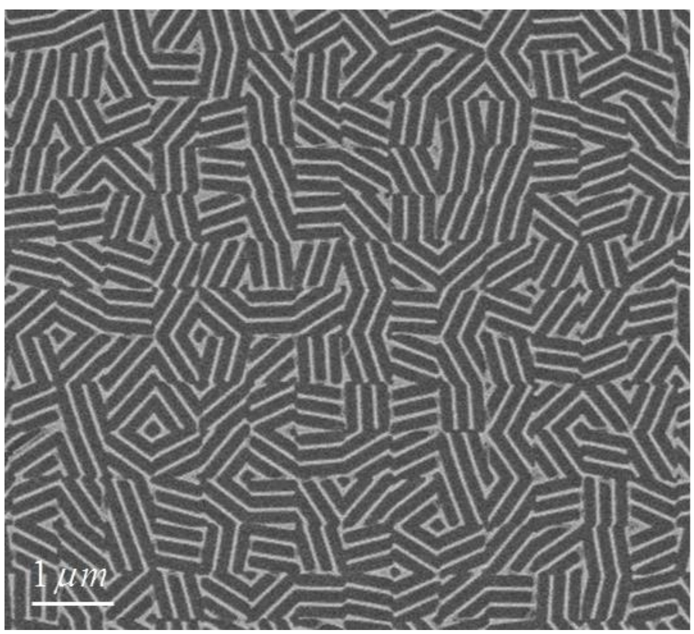

Figure S1. SEM image of the fully disordered GPM.

2. Spin-dependent momentum space calculation

The optical field emerging from a geometric phase metasurface for an arbitrary incident polarization state $|E_{in}\rangle$, is given by

$$|E_{out}\rangle = \tfrac{1}{2}\left(t_x + t_y e^{i\phi}\right)|E_{in}\rangle + \tfrac{1}{2}\left(t_x - t_y e^{i\phi}\right)\left[e^{i2\theta(x,y)}\langle\sigma_-|E_{in}\rangle|\sigma_+\rangle + e^{-i2\theta(x,y)}\langle\sigma_+|E_{in}\rangle|\sigma_-\rangle\right],$$

where $|\sigma_\pm\rangle$ stands for the spin state, and $\langle\alpha|\beta\rangle$ denotes the inner product (*12*). The last two terms are defined as the spin-flipped fields with the interaction coefficient defined by $\eta = \tfrac{1}{2}\left(t_x - t_y e^{i\phi}\right)$, where t_x, t_y are the transmission coefficients and ϕ is the phase retardation of the nano-antenna building block. The DGPMs' dimensions were determined using finite difference time domain (FDTD) simulations to obtain an efficiency of $|\eta|^2 = 0.5$ at a wavelength of $\lambda = 632.8nm$, to achieve both spin-flipped and spin-maintained states of the same field amplitude. We experimentally obtained $|\eta|^2 = 0.62$.

Using the aforementioned disordered local orientation function $\theta_\varepsilon(x,y)$, the DGPM's phase profile $\phi_g(x,y) = -2\sigma\theta_\varepsilon(x,y)$ was obtained. Calculation of the resultant momentum space intensity and phase distributions is given by

$$E_{FF}(\mathbf{k}) \propto \sum_{\mathbf{r}_j} e^{-i2\pi\mathbf{k}\cdot\mathbf{r}_j}\left\{\left(t_x + t_y e^{i\phi}\right)|E_{in}\rangle + \left(t_x - t_y e^{i\phi}\right)\left(\langle\sigma_-|E_{in}\rangle|\sigma_+\rangle e^{i2\theta_\varepsilon(\mathbf{r}_j)} + \langle\sigma_+|E_{in}\rangle|\sigma_-\rangle e^{-i2\theta_\varepsilon(\mathbf{r}_j)}\right)\right\},$$

where we regard each antenna as a local waveplate located at a discrete lattice point $\mathbf{r}_j$. The first term describes the momentum space of the spin-maintained component, while the last two terms are the spin-flipped components. The momentum space calculation of the spin-flipped component is depicted in figure S2, in a good agreement with the measured momentum space (Fig. 2D, main text).

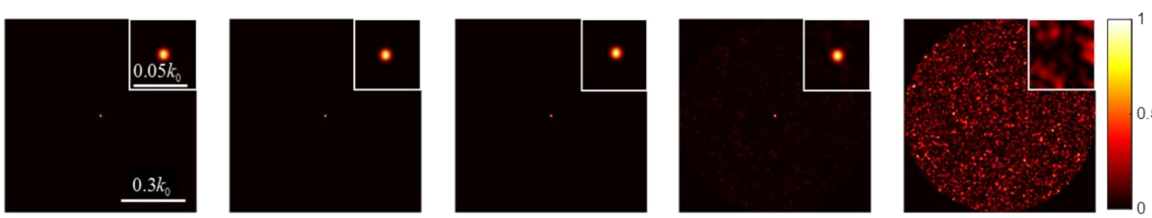

Figure S2. Momentum space calculation. Calculated momentum space intensity distributions of the spin-flipped component illuminated with spin-up for different disorder parameter (ε) values (0, 0.5, 0.85, 0.95 and 1, left to right). Insets show enlargements of the momentum space central region. Here k_0 is the wavenumber for wavelength of 633nm.

3. Polarization analysis of DGPM via Jones calculus

We used the Jones calculus to perform the polarization analysis of the optical fields in the system consisting of a DGPM, polarizers and quarter-wave plates. Using this formalism, a polarizer rotated at an angle α is described by the matrix

$$J_{Pol.}(\alpha)=\begin{pmatrix} \cos^2(\alpha) & \cos(\alpha)\sin(\alpha) \\ \cos(\alpha)\sin(\alpha) & \sin^2(\alpha) \end{pmatrix},$$

and a quarter-wave plate rotated at an angle β by

$$J_{QWP}(\beta)=\begin{pmatrix} \cos^2(\beta)+i\sin^2(\beta) & (1-i)\cos(\beta)\sin(\beta) \\ (1-i)\cos(\beta)\sin(\beta) & \sin^2(\beta)+i\cos^2(\beta) \end{pmatrix}.$$

In a similar manner, a DGPM can be described at each lattice point by the matrix

$$J_{DGPM}(\mathbf{r}_j)=\frac{\left(\mathrm{t}_x+\mathrm{t}_y e^{i\phi}\right)}{2}\begin{pmatrix} 1 & 0 \\ 0 & 1 \end{pmatrix}+\frac{\left(\mathrm{t}_x-t_y e^{i\phi}\right)}{2}\begin{pmatrix} \cos 2\theta & \sin 2\theta \\ \sin 2\theta & -\cos 2\theta \end{pmatrix}.$$

Thus, an experimental setup which includes a polarization generator, a DGPM and a polarizer-analyzer can be described by

$$E_{out}(\mathbf{r}_j,\alpha_1,\beta_1,\alpha_2,\beta_2)=J_{Pol.}(\alpha_2)\,J_{QWP}(\beta_2)\,J_{DGPM}(\mathbf{r}_j)\,J_{QWP}(\beta_1)\,J_{Pol.}(\alpha_1)\,A(\mathbf{r}_j)\,E_{in}\ .$$

Here E_{in} is the Jones vector of the incident field, and $A(\mathbf{r}_j)=\exp\left(-\left|\mathbf{r}_j\right|^2/2\sigma^2\right)$ is the field apodization. The subscripts 1 and 2 denote the circular polarizer and the polarizer-analyzer, respectively.

4. Experimental setup

Figure S3 depicts the experimental setup used to obtain our measurements. The input beam, generated by a HeNe laser source was spatially filtered and collimated. The beam's polarization state was set using a polarization generator (linear polarizer followed by a quarter-wave plate), and the beam was subsequently focused on the sample. The diffracted light was collected using an objective lens (Olympus SLMPlan 50X 0.45) and the obtained magnified image was then Fourier transformed using a second lens. The output beam's polarization state was analyzed using a polarizer-analyzer or by quarter-wave plate followed by a linear polarizer (for the weak measurement experiments). The obtained images were taken using a CMOS camera (Ximea MQ022CG-CM).

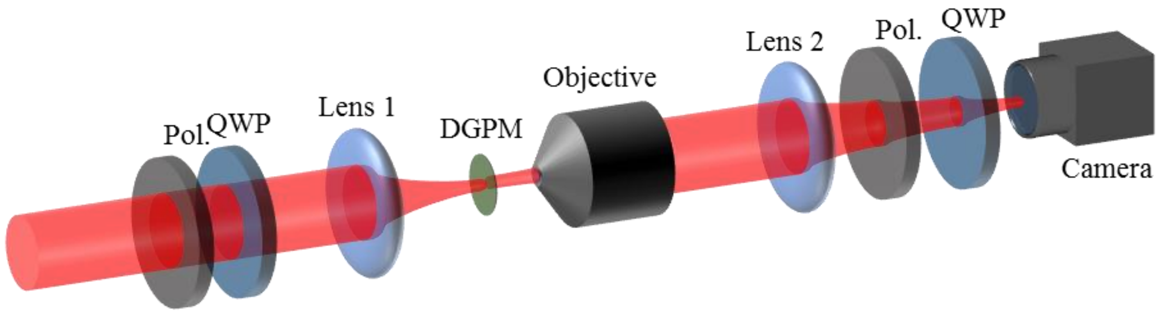

Figure S3. Experimental setup for momentum space measurements. The focal lengths for lens 1 and lens 2 are 80 and 50mm, respectively. Pol. – polarizer, QWP – quarter-wave plate.

5. Measurement of the spin-maintained component

When illuminating a DGPM with an arbitrary input polarization state, two output fields are observed – a spin-flipped component as a result of interaction with the DGPM (as depicted in figure 2D, in the main text) and a non-interacting spin-maintained component. Figure S4 shows the spin-maintained momentum space measurements of DGPMs of different disorder strength. Note, only a bright diffraction-limited spot was observed in the center of momentum space, as expected for a sub-wavelength structure.

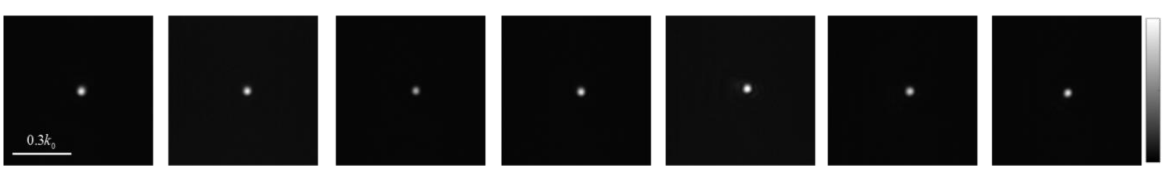

Figure S4. Measurement of the spin-maintained component. Measured momentum space intensity distributions of the spin-maintained component illuminated with spin-up for different disorder parameter (ε) values (0, 0.25, 0.5, 0.85, 0.9, 0.95 and 1, left to right).

6. Momentum space image entropy analysis

In order to evaluate the momentum space entropy, we used Shannon entropy defined as $H = -\sum_i p_i \log_2\left(p_i\right)$ (28), where p_i is the probability density function (PDF) of the momentum space which is derived from the far-field intensity distribution collected by a CMOS camera of 2048x2048 pixels. The PDF of 256 equally sized bins contains the normalized histogram counts of the image intensity distribution – pixel count per normalized intensity value. Figure S5 depicts the PDF of the calculated and measured momentum space intensities emerging from the fully disordered GPM (Fig. S5, A and B). The measured and calculated PDF of the momentum space shows good agreement with the theory obeying the negative exponential statistic $p_I\left(I\right) = \exp\left(-I/\bar{I}\right)/\bar{I}$, as predicted by Goodman, for the coherent case of a fully disordered phase (*29*). Here, p_I defined the theoretical PDF, and $I\left(\mathbf{k}\right)$ is the momentum space intensity distribution, where $\bar{I}$ is the mean intensity. Furthermore, the experimental PDFs for weak disorder values of $\varepsilon = 0.5, 0.95$ are in agreement with the calculations (Fig. S5, C to F)

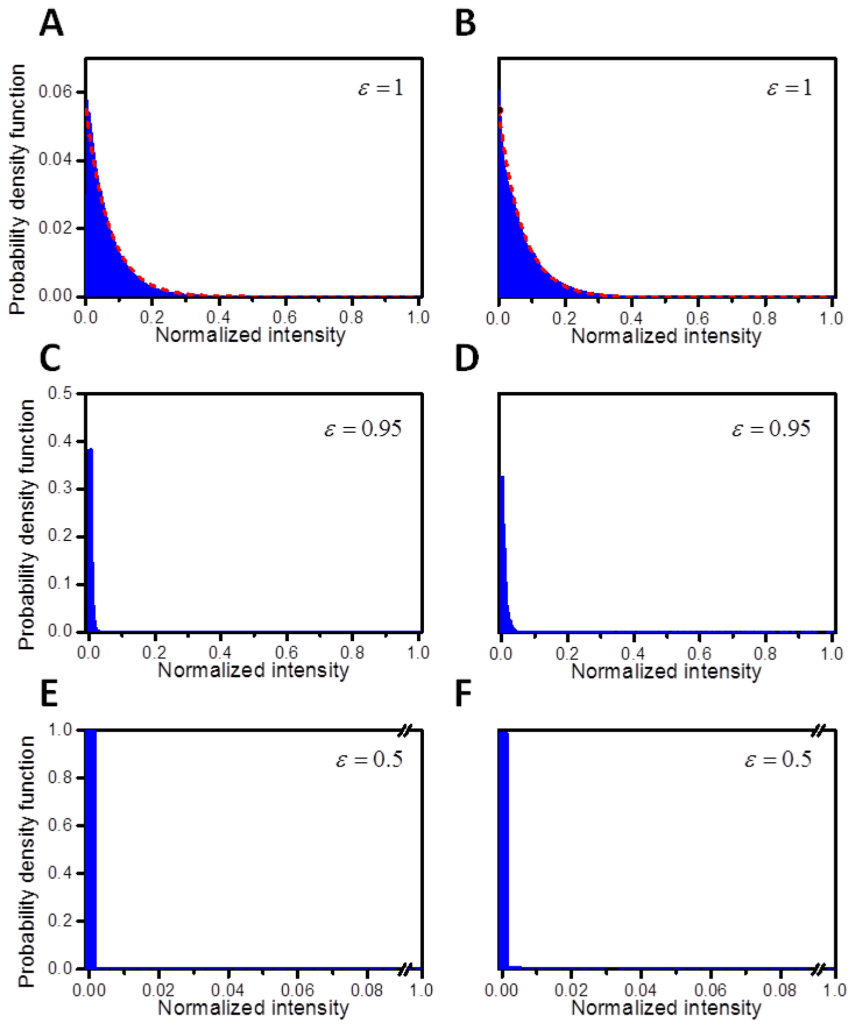

Figure S5. Probability density functions of the momentum space intensity distribution. (**A** and **B**) calculated (A) and measured (B) PDFs of the momentum space intensities emerging from a DGPM of $\varepsilon = 1$. Red lines depict the theoretical PDF obeying a negative exponent statistics. (**C** - **F**) calculated (C and E) and measured (D and F) PDFs of the momentum space intensities emerging from a DGPM of $\varepsilon = 0.5$ and $\varepsilon = 0.95$, respectively. The intensity scale at E and F is bounded to 0.1 to focus on the data at the first bin.

In order to evaluate the image entropy, we performed a summation defined by the Shannon entropy of the PDF. Figure S6 depicts the statistical distribution of the entropy over an ensemble of 100 different randomizations. The small deviations in the momentum space entropy behavior emphasize that the results are not due to a specific randomization process – any disordered GPM will obey a similar behavior, up to a standard deviation.

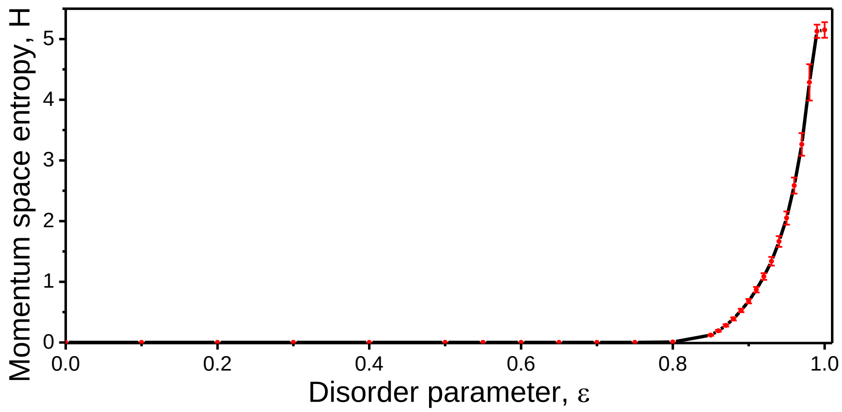

Figure S6. Momentum space image entropy statistics. Calculated momentum space image entropy over an ensemble of 100 different randomizations as a function of the disorder parameter. Red error bars depict the standard deviations.

7. Photonic transition – critical exponents

The entropy characterizes the photonic transition from weak to strong disorder. This transition can be described by a critical disorder parameter $\varepsilon_c \to 1$, and is found to obey a power law for entropy $H(\varepsilon) \propto |\varepsilon - \varepsilon_c|^{-\beta}$, where β is the critical exponent. We evaluated the entropy over an ensemble of 100 different randomizations. The calculation was performed for DGPMs of various diameters as well as for several distorted topological charges. The photonic transition was found to depend on the size of the illuminated DGPM, and also on the incident topological charge. Figure S7 depicts the change in the transition sharpness as a function of the disorder parameter for different topological charges and illumination diameters (Fig. S7, insets).

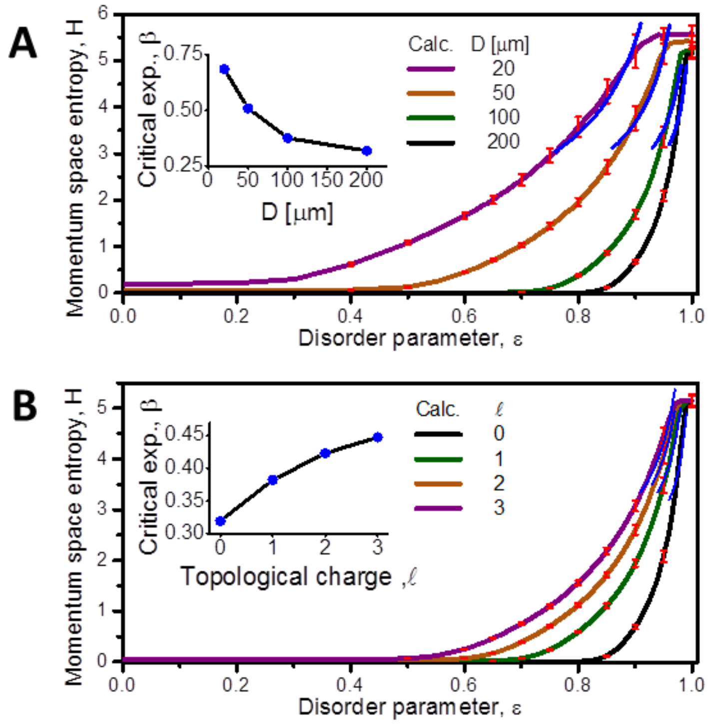

Figure S7. Power law behavior of momentum space entropy. (A) Calculated (lines) space entropies for various DGPMs of different aperture sizes (D) ranging from $20\mu m$ (purple) to $200\mu m$ (black). Inset depicts the critical exponent (β) as a function of the size of the element. (**B**) Calculated (lines) momentum space entropies for various DGPMs of different topological charges, ranging from $l=0$ (black) to $l=3$ (purple). Inset depicts the critical exponent (β) as a function of the topological charge. Blue lines depict the power law behavior near the critical point. Red error bars depict the standard deviations derived from an ensemble of 100 different randomizations.

8. Formation of topological defects – continuous phase transition

Symmetry-breaking continuous phase transitions which involve topological defects are a fundamental subject of research in many areas of physics including cosmology, particle physics, and condensed matter (26). As the system approaches the critical point of symmetry breaking from the high symmetry phase, the number of topological defects significantly increases.

In disordered geometric phase structure, topological defects based on space-variant Pancharatnam–Berry phase are formed. Such singular defects with spin-dependent orbital angular momentum are presented in figure S8; the field was calculated according to section 2 and was propagated using Huygens principle. Finite difference time domain (FDTD) simulations for fully disorder GPMs reveal the formation of spin-dependent topological defects, retrieved from the phase of the field component in the z direction.

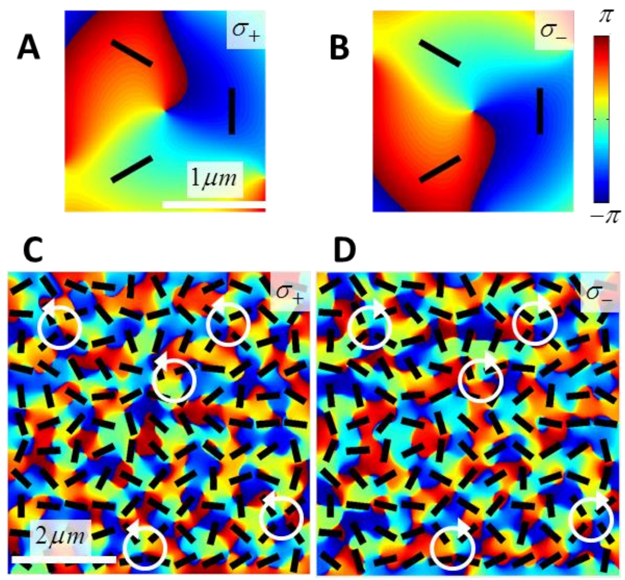

Figure S8. Formation of topological defects from DGPM. (**A** and **B**) Calculated spin-dependent phase of the field emerging from a single vortex generated by three nanoantennas. (**C** and **D**) Spin-dependent topological defects simulated by FDTD for full disorder. Black rods depict the antenna position and orientation, white circles indicate the helicity of the defects.

By superposition of the emerging spin-flipped field from the DGPMs with a plane wave of circular polarization, we calculated and experimentally observed the generation of topological defects on the interference pattern for weak ($\varepsilon = 0.25$) and strong disorder ($\varepsilon = 1$) (Fig. S9). The topological defects are manifested by a fork-shaped fringe, whereas the number of topological defects depends on the disorder parameter – strong disorder results in a significantly increased number of topological defects. The high number of defects in the vicinity of the critical point indicates a relation to continuous phase transition behavior in the system.

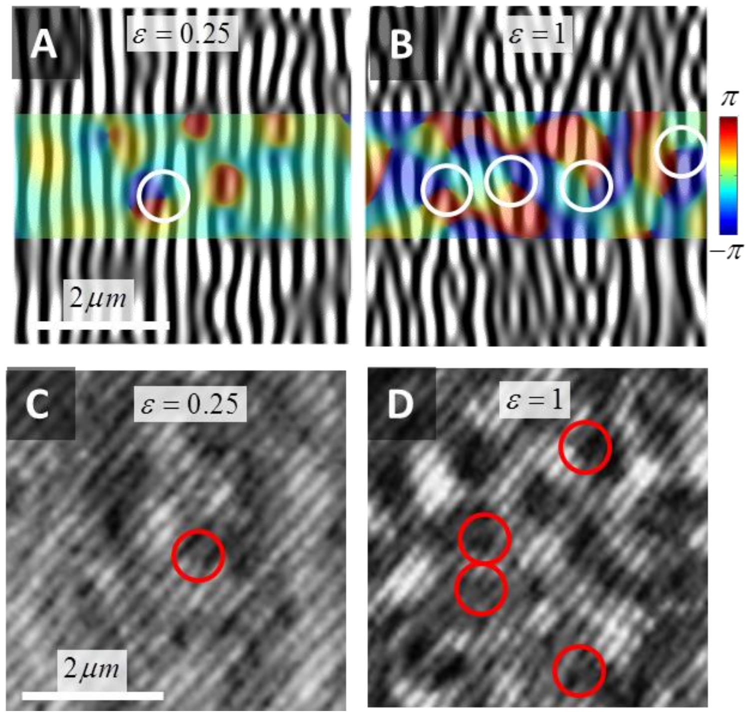

Figure S9. Observation of topological defects. (**A** - **D**) Calculation (A and B) and measurements (C and D) of the interference of a plane wave with the spin-flipped field emerging from weak and strong disordered GPMs. Colored inset (A and B) depicts the simulated (FDTD) spin-dependent phase of the field emerging from the DGPMs without the interference. White and red circles highlight the topological defects' locations, indicated by fork-shaped fringe patterns.

9. Random optical-Rashba effect – correlation functions

The experimental observation of numerous spin-split modes obtained for the fully disordered $(\varepsilon = 1)$ DGPM was analyzed using a correlation function $\left\langle I_{\sigma_+}(\mathbf{k}) I_{\sigma_-}(\mathbf{k}-\Delta\mathbf{k}) \right\rangle = \frac{1}{N}\sum_{\mathbf{k}} \left(I_{\sigma_+}(\mathbf{k}) - \overline{I_{\sigma_+}}(\mathbf{k}) \right)\left(I_{\sigma_-}(\mathbf{k}-\Delta\mathbf{k}) - \overline{I_{\sigma_-}}(\mathbf{k}-\Delta\mathbf{k}) \right)$, where $I_{\sigma_+}(\mathbf{k})$ and $I_{\sigma_-}(\mathbf{k})$ are the spin-up and spin-down momentum space intensities, and $\overline{I_{\sigma_+}}, \overline{I_{\sigma-}}$ are their mean values, respectively. Here, $\Delta\mathbf{k}$ denotes a displacement in the momentum space and $N = \sqrt{\sum_{\mathbf{k}} \left(I_{\sigma_+}(\mathbf{k}) - \overline{I_{\sigma_+}}(\mathbf{k}) \right)^2 \sum_{\mathbf{k}} \left(I_{\sigma_-}(\mathbf{k}-\Delta\mathbf{k}) - \overline{I_{\sigma_-}}(\mathbf{k}-\Delta\mathbf{k}) \right)^2}$ is a normalization factor. For $\left\langle I_{\sigma_+}(\mathbf{k}) I_{\sigma_-}(-\mathbf{k}+\Delta\mathbf{k}) \right\rangle$, a strong correlation was found (Fig.

S10, C and D), however, for $\left\langle I_{\sigma_+}(\mathbf{k}) I_{\sigma_-}(\mathbf{k}+\Delta\mathbf{k}) \right\rangle$, no correlation was found (Fig. S10, E and F).

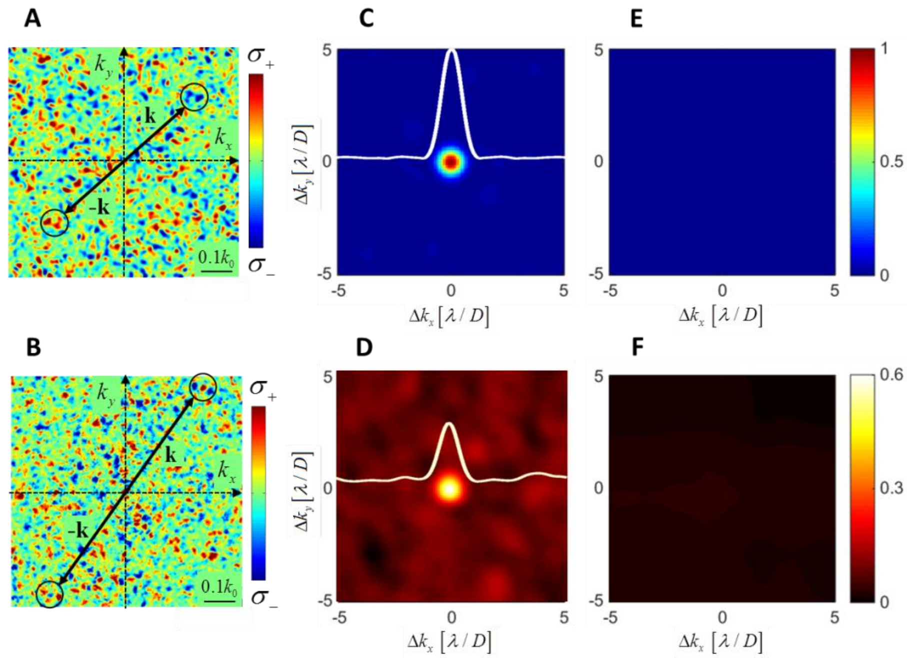

Figure S10. Spin-split random modes in the momentum space. (**A** and **B**) Calculated (A) and measured (B) difference of momentum space intensities $I_{\sigma_+}(\mathbf{k}) - I_{\sigma_-}(\mathbf{k})$ for $\varepsilon = 1$. Spin-up (σ_+) and spin-down (σ_-) are shown in red and blue, respectively. Black arrows highlight selected examples of correspondent spin-split modes. (**C** to **F**) Calculated (C and E) and measured (D and F) correlation functions of the momentum space intensities $I_{\sigma_+}(\mathbf{k})$ and $I_{\sigma_-}(-\mathbf{k})$ (C and D), and for $I_{\sigma_+}(\mathbf{k})$ and $I_{\sigma_-}(\mathbf{k})$ (E and F). A single peak, the width of which is equal to the diffraction-limited spot, is clearly observed in cross-section (C and D).

10. Linear polarization analysis of DGPMs

In order to emphasize that the phenomena originate from spin symmetry breaking rather than general polarization-dependent scattering, we studied the weak and strong disorder GPMs in the linear bases. We measured and calculated the momentum space intensity distributions of an incident linear polarization at 45° and -45° , $I_{L45}(\mathbf{k}), I_{L-45}(\mathbf{k})$, with respect to the main axis of a zero disorder GPM, whereas the emerging fields were analyzed by the orthogonal polarization states (Fig. S11, A to D). We calculated and measured the correlation functions for a full disorder structure $\left\langle I_{L45}(\mathbf{k}) I_{L-45}(-\mathbf{k}+\Delta\mathbf{k}) \right\rangle$

and $\langle I_{L45}(\mathbf{k}) I_{L-45}(\mathbf{k}+\Delta\mathbf{k})\rangle$, which resulted in a strong correlation both theoretically and experimentally (Fig. S11, E to H). These results are in contrast to spin-based observations in which for $\langle I_{\sigma_+}(\mathbf{k}) I_{\sigma_-}(\mathbf{k}+\Delta\mathbf{k})\rangle$ no correlation was found (Fig. S10, E and F); whereas for $\langle I_{\sigma_+}(\mathbf{k}) I_{\sigma_-}(-\mathbf{k}+\Delta\mathbf{k})\rangle$ there was a strong correlation as expected (Fig. S10, C and D), validating the optical Rashba effect.

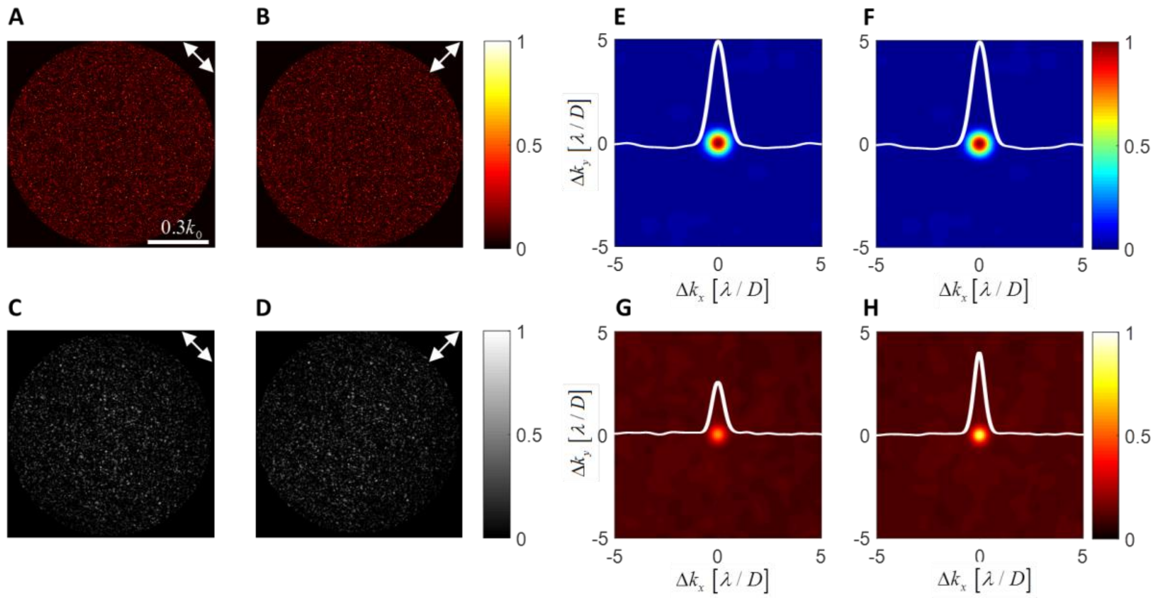

Figure S11. Correlation functions of random modes at linear polarization. (**A - D**) Calculated (A and B) and measured (C and D) momentum space intensities of the linear-polarization analyzed $I_{L45}(\mathbf{k}), I_{L-45}(\mathbf{k})$ for $\varepsilon = 1$. (**E** to **H**) Calculated (E and F) and measured (G and H) correlation functions $\langle I_{L45}(\mathbf{k}) I_{L-45}(-\mathbf{k}+\Delta\mathbf{k})\rangle$ and $\langle I_{L45}(\mathbf{k}) I_{L-45}(\mathbf{k}+\Delta\mathbf{k})\rangle$, of the momentum space intensities. A single peak, the width of which is equal to the diffraction-limited spot, is clearly observed in cross-sections.

In order to show that the symmetry breaking in weak DGPMs is spin-based rather than a result of general polarization phenomena, we calculated the center of the momentum space intensity distributions in the weak disorder for linearly polarized-analyzed states of $I_{L45}(\mathbf{k}), I_{L-45}(\mathbf{k})$ (Fig. S12, A and B) and compared it to the spin basis $I_{\sigma_+}(\mathbf{k}), I_{\sigma_-}(\mathbf{k})$ (Fig. S12, D and E). The obtained results for the different linear polarizations are identical as depicted by $I_{L45}(\mathbf{k}) - I_{L-45}(\mathbf{k})$ (Fig. S12C), and are in contrast to the spin-based calculation of $I_{\sigma_+}(\mathbf{k}) - I_{\sigma_-}(\mathbf{k})$ (Fig. S12F), in which a PSHE is obtained.

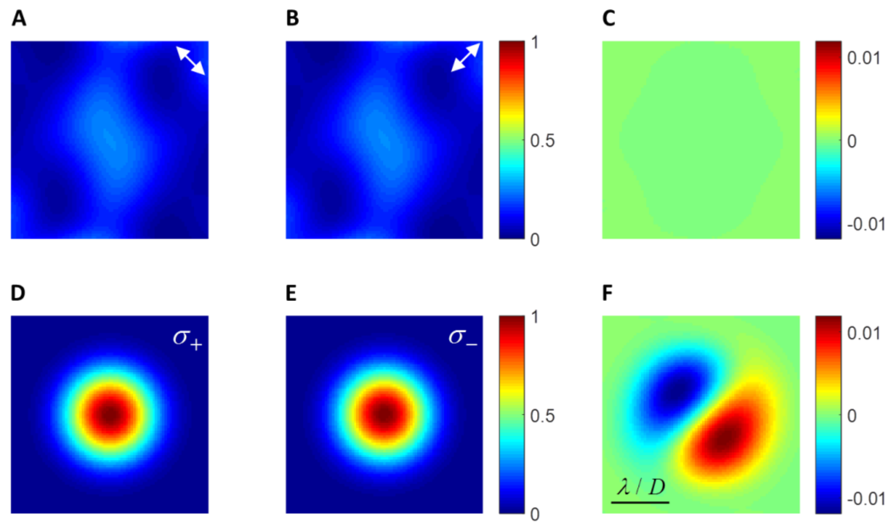

Figure S12. Linear polarization symmetry of weak disorder. (**A - C**) Calculated intensity patterns $I_{L45}(\mathbf{k})$ (A) and $I_{L-45}(\mathbf{k})$ (B), and the difference between them (C). (**D - F**) Calculated intensity patterns $I_{\sigma_+}(\mathbf{k})$ (A) and $I_{\sigma_-}(\mathbf{k})$ (B), and the difference between them (F).

11. PSHE for extremely small disorder

We studied the onset of the PSHE, namely the transition from an ordered structure $(\varepsilon = 0)$ to a structure having a small amount of disorder $\varepsilon \to 0$. As shown in figure S13, even for extremely small disorder, PSHE is still obtained.

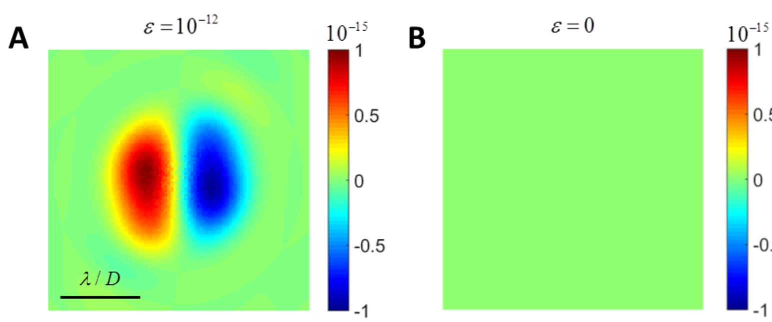

Figure S13. **Photonic transition from order to weak disorder. (A)** Calculated difference of the momentum space intensities $I_{\sigma_+}(\mathbf{k}) - I_{\sigma_-}(\mathbf{k})$, demonstrating the PSHE emerging from an extremely weakly disordered GPM, $\varepsilon = 10^{-12}$. (**B**) The absence of PSHE in an ordered GPM. Red and blue represent the amount of right and left circular polarization, respectively.

12. Observation of the photonic spin Hall effect via weak measurement

The experimental observation of the PSHE was achieved using quantum weak measurement techniques to enable an amplification of the sub-diffraction-limit beam-shift (*20*,*23*, *24*). By utilizing the weak measurement technique we measured a separation on the order of the diffraction-limited spot for DGPMs of different disorder strengths with on- axis illumination (Fig. S14).

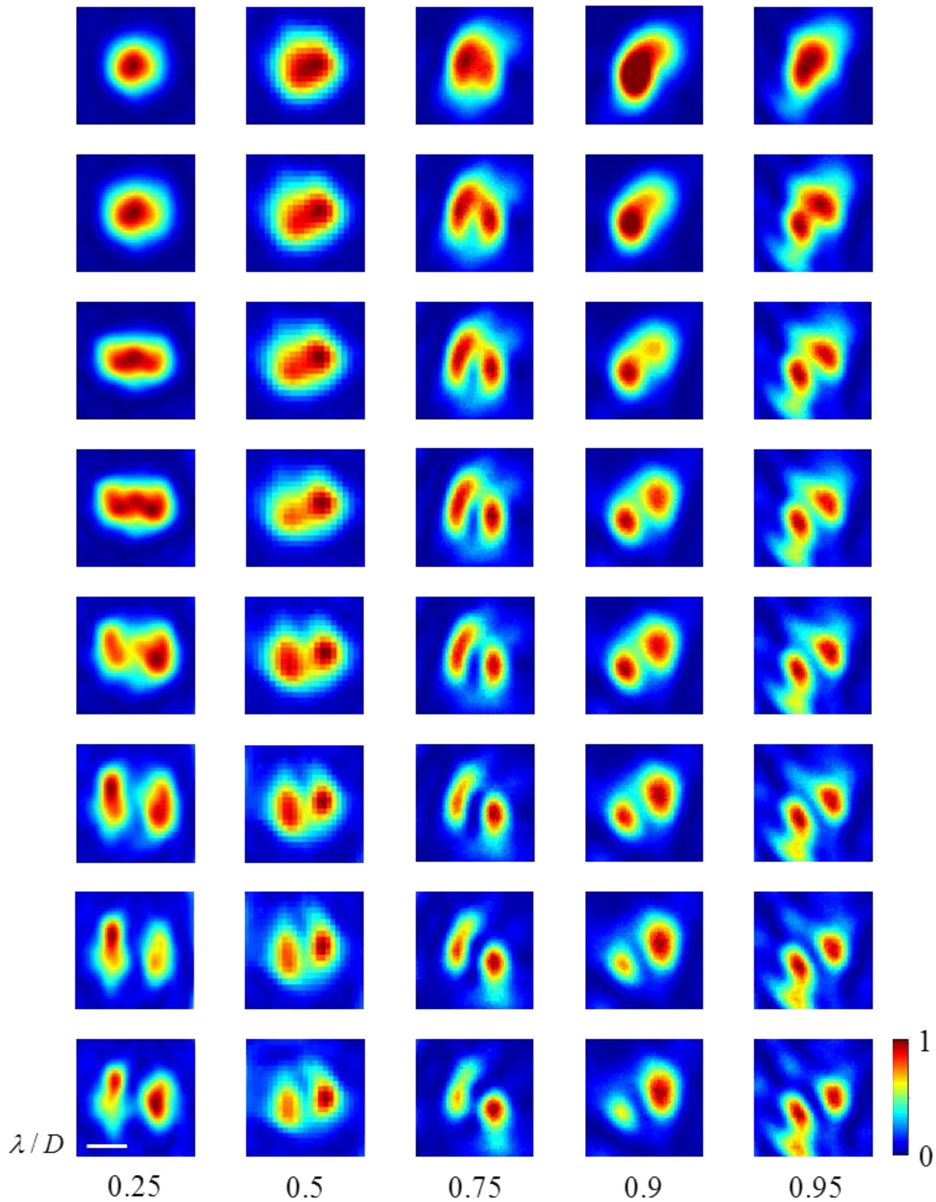

Figure S14. Weak measurement. Experimental amplification of the PSHE obtained via weak measurement for a DGPM of $\varepsilon = 0.25, 0.5, 0.75, 0.9, 0.95$. Images are taken at various polarizer-analyzer angles starting at 0 (bottom, cross polarization) and increasing with steps of 0.1, 0.1, 0.25, 0.5, and 1 degrees, respectively.

13. Weak measurement of singular points

We studied the instability of distorted high-order singularities via weak measurement of singular points. By the projection of both orthogonal spin-states – the spin-flipped distorted vortex and the spin-maintained Gaussian beam – onto an elliptical polarization state, weak measurement of singular points was achieved. We compared the obtained results with calculations by use of Jones calculus. Figure S15 depicts the breaking of an OAM carrying beam of $l = 3$ into generic singularities of $l = 1$ at fixed post-selection polarizations, demonstrating disorder strength-dependent separation – repulsive vortex interaction.

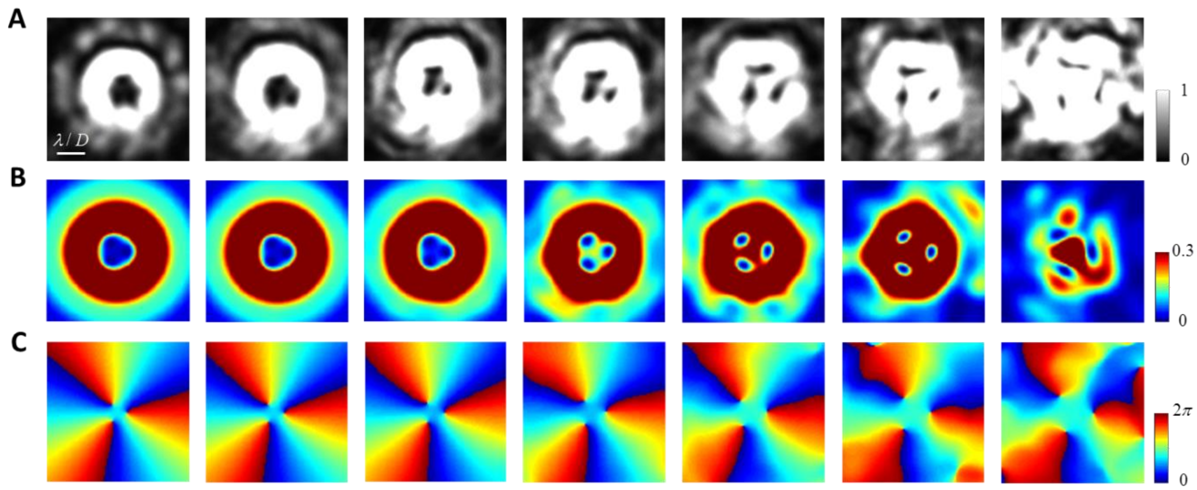

Figure S15. Weak measurement of singular points. (**A** – **C**) Saturated intensity profiles of the weak measurement of the singularities' separation for $\varepsilon = 0$, 0.25, 0.5, 0.75, 0.85, 0.9 and 0.95 (left to right) and a topological charge $l = 3$; top – measured intensity (A), middle – calculated intensity (B), and bottom – calculated phase (C). Polarizer-analyzer was set to a fixed deviation angle of 2° from the spin-flip state.

14. Spin-dependent imaging through a DGPM

We demonstrate spin-dependent imaging using a transparency-imprinted logo of the Technion, as depicted by figure S16A. When this transparency is illuminated with circularly polarized light, the spin-maintained non-interacting component is undisturbed and imaged as expected (Fig. S16B) while the spin-flipped imaging component breaks down into numerous scattered modes (Fig. S16C).

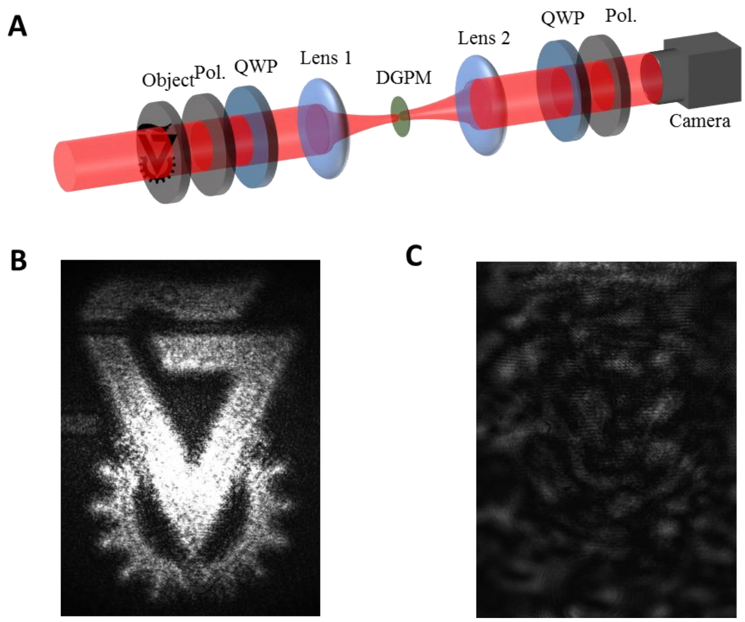

Figure S16. Imaging through DGPM. (**A**) Experimental setup schematic of the imaging system with an input transparency-imprinted logo of the Technion. The focal length for both lenses is 50mm. Pol. – polarizer, QWP – quarter-wave plate. (**B** and **C**) Spin-maintained (B) and spin-flipped (C) components of the resulting images.

15. Photonic transition due to defects in the geometric phase

In the main text we described the transition as a function of the disorder strength (ε) implemented at all lattice points. An electronic spin Hall effect induced by impurities (4) inspires one to investigate the photonic transport due to defects in the geometric phase. Therefore, we studied the PSHE and the momentum space entropy that emerged due to variation in the number of lattice points that possessed a fully disordered geometric phase. For this purpose, we randomly selected nanoantennas from a uniform GPM to have a fully disordered orientation, where the density of the defects constituted a portion of the antennas comprising the DGPM (Fig. S17, A). The density of the geometrical phase defects (ξ) is defined as the ratio between the number of randomly selected nanoantennas and the total number of points in the lattice. Using the methods described in Section 2, we calculated the momentum space entropy of DGPMs of 100µm diameter at different densities of defect, ranging from 0 to 1, and observed the photonic transition (Fig. S17, B and C). Importantly, the transition from PSHE to Rashba effect was obtained at geometric phase defect densities of $\xi < 1$ to $\xi = 1$, respectively (Fig. S17, C insets).

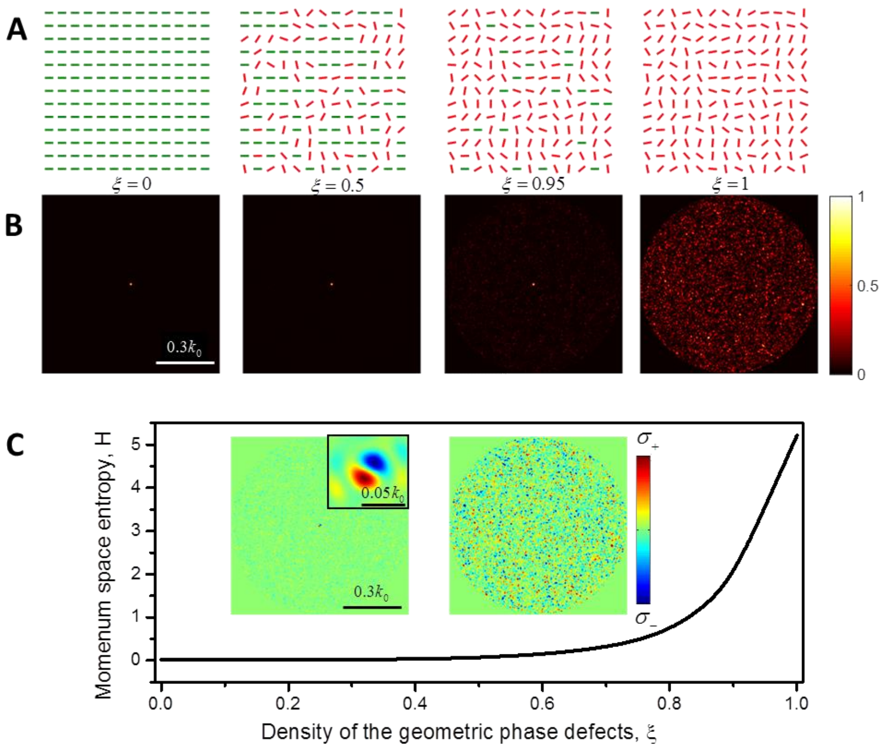

Figure S17. Momentum space entropy due to geometric phase defects. (**A**) DGPM structures with defects in the geometric phase; green and red antennas represent non-distorted orientation and defects, respectively. (**B**) Calculated momentum space intensity distributions of the spin-flipped component. Here k_0 is the wavenumber for wavelength of 633nm. (**C**) Calculated momentum space image entropy as a function of the geometric phase defect density. Colored insets depict the calculated difference of the momentum space intensities $I_{\sigma_+}(\mathbf{k})-I_{\sigma_-}(\mathbf{k})$, demonstrating the PSHE emerging from moderated density of the geometrical phase defects $0<\xi<1$ (left) and Rashba effect for $\xi=1$ (right).

16. Metallic DGPM

In the main text we demonstrated the photonic transition phenomena via dielectric DGPMs. Here we show that the transitional effect is also obtained from a metallic DGPM based on local plasmon resonances. The coupling of light to this type of metasurface is supported by plasmonic resonances originating from the local plasmonic mode of a nano-hole (nanoantenna) within a structured metal surface. Figure S18 depicts the scanning electron microscope images of metallic DGPMs of 50μm diameter, fabricated using a Ga^+ focused ion beam, where holes of 80-by-220-nm^2 rod apertures were perforated in a 200nm-thick Au film.

We illuminated the metallic DGPMs of different ε with circularly polarized light from a 633nm He-Ne laser, and measured the emerging far-field spin-flipped component. A bright spot was observed in the center of momentum space for disorder parameter values up to $\varepsilon = 0.95$. When the disorder parameter approached unity numerous modes spanning the momentum space were observed. We quantify this transitional effect via the momentum space image entropy from the far-field measurements and observed a steep increase in the vicinity of full disorder, in agreement with the calculation (Fig. S18A). Moreover, we demonstrate the photonic transitions from weak to strong disorder by calculating the PSHE for $\varepsilon = 0.8$ and random optical-Rashba effect for $\varepsilon = 1$, obtained from these structures (Fig. S18, E and F).

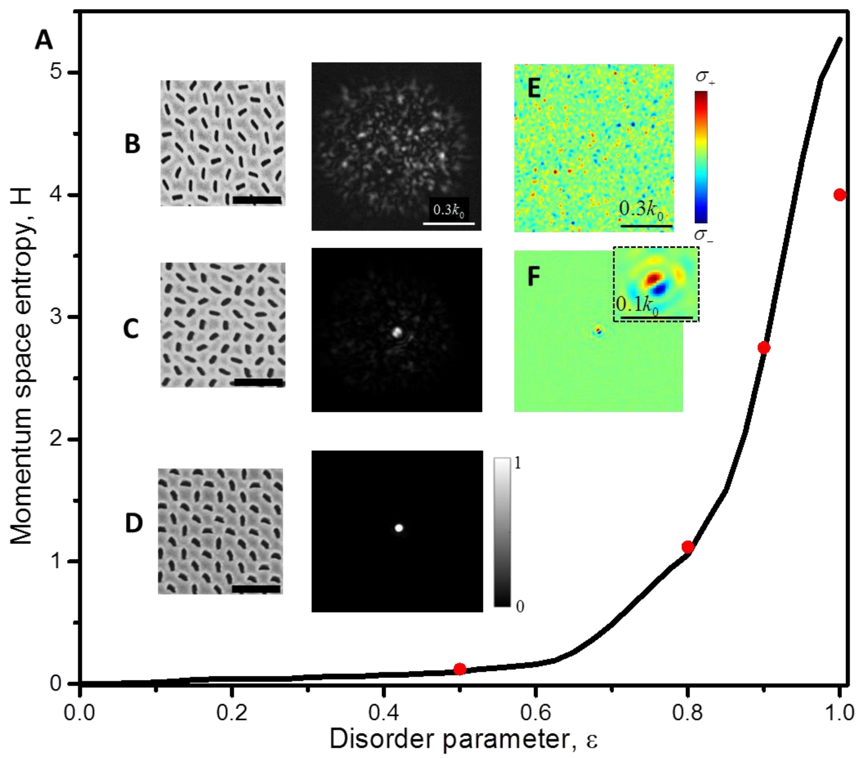

Figure S18. Photonic transition for metallic DGPMs. (**A**) Calculated (line) and measured (red circles) momentum space image entropy. (**B** – **D**) Scanning electron microscope images and the corresponding measured momentum space intensity distributions of the spin-flipped component illuminated with spin-up for $\varepsilon = 1$ (B), $\varepsilon = 0.8$ (C) and $\varepsilon = 0.5$ (D). Here, the bar size is 1μm and k_0 is the wavenumber for a wavelength of 633nm. (**E** and **F**) The difference in the calculated momentum space intensities $I_{\sigma_+}(\mathbf{k}) - I_{\sigma_-}(\mathbf{k})$ shows the Rashba effect for $\varepsilon = 1$ (E) and PSHE for $\varepsilon = 0.8$ (F).

17. Photonic transition of different lattice symmetry

Throughout the paper, the DGPMs were based on a subwavelength cubic lattice. Here, we study the photonic transition emerging from the subwavelength lattices having different symmetry. A comparison of the momentum entropy of DGPMs based on cubic, hexagonal and Kagome lattices with equal diameters (200μm) and number of nanoantennas was performed. The calculation shows a similar behavior of the momentum space entropy for the different lattices (Fig. S19).

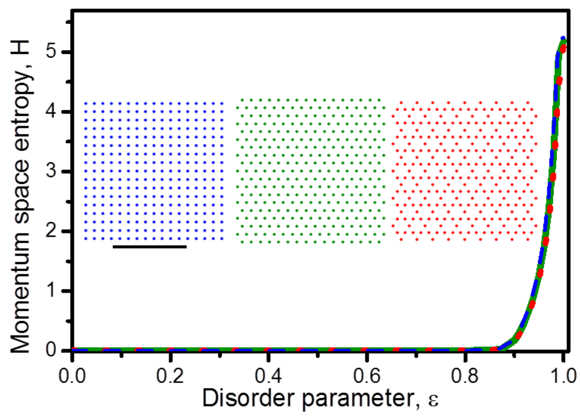

Figure S19. Momentum space entropy of DGPMs based on different lattices. Calculated momentum space entropy of cubic (blue), hexagonal (green) and Kagome (red) lattices as a function of the disorder parameter. The bar size is 2μm.

References and Notes

1. *50 Years of Anderson Localization*, E. Abrahams, Ed. (World Scientific, Singapore, 2010).

2.M. V. Berry, Quantal phase factors accompanying adiabatic changes. *Proc. R. Soc. London Ser. A* **392**, 45–57 (1984). doi:10.1098/rspa.1984.0023

3. M. I. Dyakonov, V. I. Perel, Current-induced spin orientation of electrons in semiconductors. *Phys. Lett. A* **35**, 459–460 (1971). doi:10.1016/0375-9601(71)90196-4

4. J. Sinova, S. O. Valenzuela, J. Wunderlich, C. H. Back, T. Jungwirth, Spin Hall effects. *Rev. Mod. Phys.* **87**, 1213–1260 (2015). doi:10.1103/RevModPhys.87.1213

5. A. Apostol, A. Dogariu, Spatial correlations in the near field of random media. *Phys. Rev. Lett.* **91**, 093901 (2003). doi:10.1103/PhysRevLett.91.093901 Medline

6. M. Segev, Y. Silberberg, D. Christodoulides, Anderson localization of light. *Nat. Photonics* **7**, 197–204 (2013). doi:10.1038/nphoton.2013.30

7. D. S. Wiersma, Disordered photonics. *Nat. Photonics* **7**, 188–196 (2013). doi:10.1038/nphoton.2013.29

8. H. H. Sheinfux, Y. Lumer, G. Ankonina, A. Z. Genack, G. Bartal, M. Segev, Observation of Anderson localization in disordered nanophotonic structures. *Science* **356**, 953–956 (2017). doi:10.1126/science.aah6822 Medline

9. A. Pors, F. Ding, Y. Chen, I. P. Radko, S. I. Bozhevolnyi, Random-phase metasurfaces at optical wavelengths. *Sci. Rep.* **6**, 28448 (2016). doi:10.1038/srep28448 Medline

10. K. Y. Bliokh, F. Nori, Transverse and longitudinal angular momenta of light. *Phys. Rep.* **592**, 1–38 (2015). doi:10.1016/j.physrep.2015.06.003

11. K. Y. Bliokh, F. J. Rodríguez-Fortuño, F. Nori, A. V. Zayats, Spin–orbit interactions of light. *Nat. Photonics* **9**, 796–808 (2015). doi:10.1038/nphoton.2015.201

12. Z. Bomzon, G. Biener, V. Kleiner, E. Hasman, Space-variant Pancharatnam-Berry phase optical elements with computer-generated subwavelength gratings. *Opt. Lett.* **27**, 1141–1143 (2002). doi:10.1364/OL.27.001141 Medline

13. V. M. Shalaev, Optical negative-index metamaterials. *Nat. Photonics* **1**, 41–48 (2007). doi:10.1038/nphoton.2006.49

14. E. T. F. Rogers, J. Lindberg, T. Roy, S. Savo, J. E. Chad, M. R. Dennis, N. I. Zheludev, A super-oscillatory lens optical microscope for subwavelength imaging. *Nat. Mater.* **11**, 432–435 (2012). doi:10.1038/nmat3280 Medline

15. X. Yin, Z. Ye, J. Rho, Y. Wang, X. Zhang, Photonic spin Hall effect at metasurfaces. *Science* **339**, 1405–1407 (2013). doi:10.1126/science.1231758 Medline

16. N. Shitrit, I. Yulevich, E. Maguid, D. Ozeri, D. Veksler, V. Kleiner, E. Hasman, Spin-optical metamaterial route to spin-controlled photonics. *Science* **340**, 724–726 (2013). doi:10.1126/science.1234892 Medline

17. E. I. Rashba, Properties of semiconductors with an extremum loop. 1. Cyclotron and combinational resonance in a magnetic field perpendicular to the plane of the loop. *Sov. Phys. Solid State* **2**, 1109 (1960).

18. K. Ishizaka, M. S. Bahramy, H. Murakawa, M. Sakano, T. Shimojima, T. Sonobe, K. Koizumi, S. Shin, H. Miyahara, A. Kimura, K. Miyamoto, T. Okuda, H. Namatame, M. Taniguchi, R. Arita, N. Nagaosa, K. Kobayashi, Y. Murakami, R. Kumai, Y. Kaneko, Y. Onose, Y. Tokura, Giant Rashba-type spin splitting in bulk BiTeI. *Nat. Mater.* **10**, 521–526 (2011). doi:10.1038/nmat3051 Medline

19. N. Dahan, Y. Gorodetski, K. Frischwasser, V. Kleiner, E. Hasman, Geometric doppler effect: Spin-split dispersion of thermal radiation. *Phys. Rev. Lett.* **105**, 136402 (2010). doi:10.1103/PhysRevLett.105.136402 Medline

20. Y. Aharonov, D. Z. Albert, L. Vaidman, How the result of a measurement of a component of the spin of a spin-1/2 particle can turn out to be 100. *Phys. Rev. Lett.* **60**, 1351–1354 (1988). doi:10.1103/PhysRevLett.60.1351 Medline

21. D. Lin, P. Fan, E. Hasman, M. L. Brongersma, Dielectric gradient metasurface optical elements. *Science* **345**, 298–302 (2014). doi:10.1126/science.1253213 Medline

22. See supplementary materials.

23. O. Hosten, P. Kwiat, Observation of the spin hall effect of light via weak measurements. *Science* **319**, 787–790 (2008). doi:10.1126/science.1152697 Medline

24. K. Y. Bliokh, D. Smirnova, F. Nori, OPTICS. Quantum spin Hall effect of light. *Science* **348**, 1448–1451 (2015). doi:10.1126/science.aaa9519 Medline

25. M. V. Berry, R. G. Chambers, M. D. Large, C. Upstill, J. C. Walmsley, Wavefront dislocations in the Aharonov-Bohm effect and its water wave analogue. *Eur. J. Phys.* **1**, 154–162 (2000). doi:10.1088/0143-0807/1/3/008

26. S. Ducci, P. L. Ramazza, W. González-Viñas, F. T. Arecchi, Order parameter fragmentation after a symmetry-breaking transition. *Phys. Rev. Lett.* **83**, 5210–5213 (1999). doi:10.1103/PhysRevLett.83.5210

27. C. Riek, D. V. Seletskiy, A. S. Moskalenko, J. F. Schmidt, P. Krauspe, S. Eckart, S. Eggert, G. Burkard, A. Leitenstorfer, Direct sampling of electric-field vacuum fluctuations. *Science* **350**, 420–423 (2015). doi:10.1126/science.aac9788 Medline

28. C. E. Shannon, A mathematical theory of communication. *Bell Syst. Tech. J.* **27**, 379–423 (1948). doi:10.1002/j.1538-7305.1948.tb01338.x

29. J. W. Goodman, *Statistical Optics* (Wiley-Interscience, New York, 2000).